Activating Multi-Electron Reaction of NASICON-structured Cathodes towards Unprecedented Energy Density for Sodium-Ion Batteries

Mingzhe Chen[†,¶], *Weibo Hua*[‡,¶,Γ], *Jin Xiao*[§], *Jiliang Zhang*[†], *Vincent Wing-hei Lau*[†], *Mihui Park*[Δ], *Gi-Hyeok Lee*[Δ], *Suwon Lee*[†], *Wanlin Wang*[#], *Jian Peng*[#], *Liang Fang*[Δ], *Limin Zhou*[†], *Chung-Kai Chang*[//], *Yusuke Yamauchi*[€], *Shu-Lei Chou*[#] *and Yong-Mook Kang*[*,†,⊥]

[†]Department of Materials Science and Engineering, Korea University, Seoul 02841, Republic of Korea

[‡]Institute for Applied Materials-Energy Storage Systems (IAM-ESS), Karlsruhe Institute of Technology (KIT), 76344 Eggenstein-Leopoldshafen, Germany

[Γ]*School of Chemical Engineering and Technology, Xi'an Jiaotong University, Xi'an, Shaanxi, 710049, China*

[§]School of Science, Hunan University of Technology, Zhuzhou, 412007, China

[Δ]Department of Energy and Materials Engineering, Dongguk University-Seoul, 04620 Seoul, Republic of Korea

[#]Institute for Superconducting and Electronic Materials (ISEM), Australian Institute for Innovative Materials (AIIM), University of Wollongong, Innovation Campus Squires Way, North Wollongong, NSW 2522, Australia

[//]National Synchrotron Radiation Research Center, Hsinchu 30076 Taiwan, R. O. C.

[€]School of Chemical Engineering and Australian Institute for, Bioengineering and Nanotechnology (AIBN), The University of Queensland, Brisbane, QLD, 4072 Australia

[⊥]KU-KIST Graduate School of Converging Science and Technology, Korea University, Seoul, 02841 Republic of Korea

KEYWORDS: multi-electron reaction, high potential, energy density, NASICON-type material, sodium-ion battery

ABSTRACT: The increasing demand to efficiently store and utilize the electricity from renewable energy resources in a sustainable way has boosted the request for sodium-ion battery technology due to the high abundance of sodium source worldwide. Na superionic conductor (NASICON)-structured cathodes with robust polyanionic framework have been intriguing because of their open 3D structure and superior thermal stability. The ever-increasing demand for higher energy densities with NASICON-structured cathodes motivates us to activate multi-electron reactions, thus utilizing the third sodium ion toward higher voltage and larger capacity, both of which have been the bottlenecks for commercializing sodium-ion batteries. A doping strategy with Cr inspired by first-principal calculations enables the activation of multi-electron redox reactions of the redox couples V^{2+}/V^{3+}, V^{3+}/V^{4+} and V^{4+}/V^{5+}, resulting in remarkably improved energy density even compared to the layer structured oxides and Prussian blue analogues. This work also comprehensively clarifies the role of the Cr dopant during sodium storage and the valence electron transition process of both V and Cr. Our findings highlight the importance of broadly applicable doping strategy for achieving multi-electron reaction of NASICON-type cathodes with higher energy densities in sodium-ion batteries.

1. Introduction

The practical application of renewable energy sources such as solar and wind energy strongly has boosted a rapidly increasing demand for high performance electrochemical energy storage and conversion devices.[1,2] Although lithium-ion batteries (LIBs) have achieved tremendous success in commercially viable electric vehicles (EVs) and portable devices with its satisfactory energy densities, the limited lithium availability and unevenly distributed nature of lithium resources remain critical against the urgent demand of battery systems for large-scale, cost-effective energy storage systems (EESs).[3,4] Sodium-ion batteries (SIBs) are considered as the promising candidate for grid-scale energy storage because of their high abundance and worldwide availability.[5,6] In order to achieve competitive performance of SIBs, however, tremendous efforts are still in demand for developing more robust and higher energy electrodes,[7-9]

especially the cathodes, based on comprehensive understanding of the sodium storage mechanisms involved.[10,11]

Various types of cathodes have been investigated till now, including layered sodium transition-metal oxides[8,12-14] polyanions[15-19] and alkali-metal hexacyanometalates.[20-23] Among them, the polyanionic materials are considered as one of the most important candidates in recent years with extensive investigations for practical applications.[5,24,25] The transition-metal phosphate with the sodium super ionic conductor (NASICON) structures play decisive roles in the polyanionic families since they possess robust three-dimensional (3D) frameworks, small volume change during cycling and high reversible capacity.[24,26] Moreover, its open structure can provide 3D Na^+ diffusion pathways,[27] which is an important factor for realizing high-rate performance, and their inherently strong inductive effect between the phosphates and transition metals can supply relatively higher working potentials vs. Na^+/Na than that of other cathodes with similar redox couples.[28-30] Besides, most of the NASICON-type electrodes rarely undergo complex phase transition reaction during sodium storage, resulting in satisfactory cycling stability, which is an important factor for large-scale EESs.[28,31-34] Among them, $Na_3V_2(PO_4)_3$ can be regarded as the prevalent representative material, since it possesses relatively high working voltage of around 3.4 V and a theoretical capacity of 117 mAh g^{-1} with excellent rate performance despite its relatively low electrical conductivity.[35-37]

Another important parameter for EESs is the energy density, which is mainly subjected to two electrochemical properties of cathodes, the working potential and specific capacity.[38] Increasing the number of participating electrons in the overall reaction is one of the effective approaches for improving the reversible specific capacity.[9] Considering the benefits that the NASICON-structured $Na_3V_2(PO_4)_3$ possesses, it is of great importance to activate more than two electrons in the overall redox reaction, since vanadium is known to have at least four stable oxidation states (2+, 3+, 4+ and 5+).[39-42] This route is also related to the accessibility of the third sodium ion in the $Na_3V_2(PO_4)_3$ structure, which has been commonly considered to transform into a thermodynamically unstable phase within typically used electrolytes.[9] Interestingly, Jin *et al.* recently discovered that a proper amount of transition metal of Cr doped into the VO_6 octahedra can activate the V^{4+}/V^{5+} redox couple in a non-aqueous electrolyte.[40] Their pioneering findings have shed light upon the new approach for pursuing higher energy densities. Mai *et al.*[39] and Ceder *et al.*[43] also have reached the three-electron reaction by using Mn as the redox centre; however, their cycling stabilities are sacrificed since the John-Teller effect of Mn seems inevitable during the whole reaction.[44] Therefore, V-based NASICON-type cathodes looks most promising because of its satisfactory cycling stability. It has been confirmed that proper amount of Cr doping in V-based oxides is effective to activate the third sodium ion;[45] however, the real reason why the Cr dopant in VO_6 octahedra can trigger higher redox potentials of vanadium still remains elusive, and we believe this kind of strategy can be expanded to other structures as well. This inspired us to undertake a deeper exploration of vanadium oxidation at higher voltage.

Here in this work, we have comprehensively and systemically investigated how Cr-doping in NASICON-type cathodes can fully activate the three-electron reaction of vanadium in non-aqueous electrolyte. The fast and stable electrochemical performance is achieved at various current densities with the help of uniformly coated carbon layer on micro/nano particles. In the wide voltage window of 4.2-1.0 V, the overall energy density has been successfully improved at all C-rates compared to the pristine electrode. By employing advanced characterization techniques, we have also determined that a unique solid-solution reaction occurs during sodium storage, which can render more smooth sodium diffusion process. This discovery is also verified by *ab* initio calculations. Cr as the electrochemically inactive dopant in the NASICON structure can contribute to a decreased forbidden band gap, and the unpaired electron of Cr in its 3*d* orbital is a key for successfully triggering the higher voltage reaction with the V^{4+}/V^{5+} redox couple. Our findings offer unprecedented insights into the development of highly performing sodium ion systems, and we believe that this inactive dopant strategy also can be applied in other types of materials for activating potentially higher energy densities as well.

2. Results and discussion

A sol-gel method was adopted for synthesizing the proposed $Na_3V_{1.5}Cr_{0.5}(PO_4)_3$ NASICON-type cathode by annealing the gel precursor in Ar atmosphere for 24 h with an intermediate grinding. **Figure 1a** shows the synchrotron powder diffraction pattern (λ = 0.687665 Å) of $Na_3V_{1.5}Cr_{0.5}(PO_4)_3$ with good weighted profile R factor (wR_p = 6.124 %). All the observed peaks agree with the pattern of typical NASICON structure (Figure 1b) with a rhombohedral *R*-3*c* space group (a = b = 8.7124(6) Å, c = 21.8147(9) Å), yielding a volume V = 1434.045(2) $Å^3$ per unit cell. The smaller value of *a* is consistent with the smaller ionic radius of Cr^{3+} (0.615 Å) relative to that of V^{3+} (0.64 Å). No other phase was found, indicating the phase purity of $Na_3V_{1.5}Cr_{0.5}(PO_4)_3$. The doped Cr atoms are found to be randomly distributed in the original V octahedra site by the Rietveld refinement results. In its open 3-dimensional (3D) framework, the PO_4 tetrahedra is connected with three CrO_6/VO_6 octahedra by sharing the O atom, therefore sufficient sodium diffusion channels can be created. Detailed crystallographic data from the Rietveld refinement are provided in Table S1. Besides, in order to fully understand why Cr-doping can activate V^{4+}/V^{5+} redox couple, we also synthesized the undoped $Na_3V_2(PO_4)_3$, and its Rietveld refinement results and detailed crystallographic data are provided in **Figure S1** and Table S2, which will be discussed in details later on. Thermogravimetric (TG) analysis for both $Na_3V_{1.5}Cr_{0.5}(PO_4)_3$ and its precursor are shown in **Figure S2**. Almost no weight loss can be observed after 600 ℃ in Ar atmosphere, and its carbon content is determined to be 5.55 % of the final product.

The surface information regarding the valence of V and Cr are preliminarily detected by X-ray photoelectron spectroscopy (XPS), which is displayed in Figure 1c and d. The $2p_{1/2}$ and $2p_{2/3}$ orbitals of both Cr and V can be observed and deconvoluted, and their corresponding bonding energies are all close to the theoretical values for Cr^{3+} and V^{3+}. The full XPS survey is shown in **Figure S3**a with all the identified elements, and the C

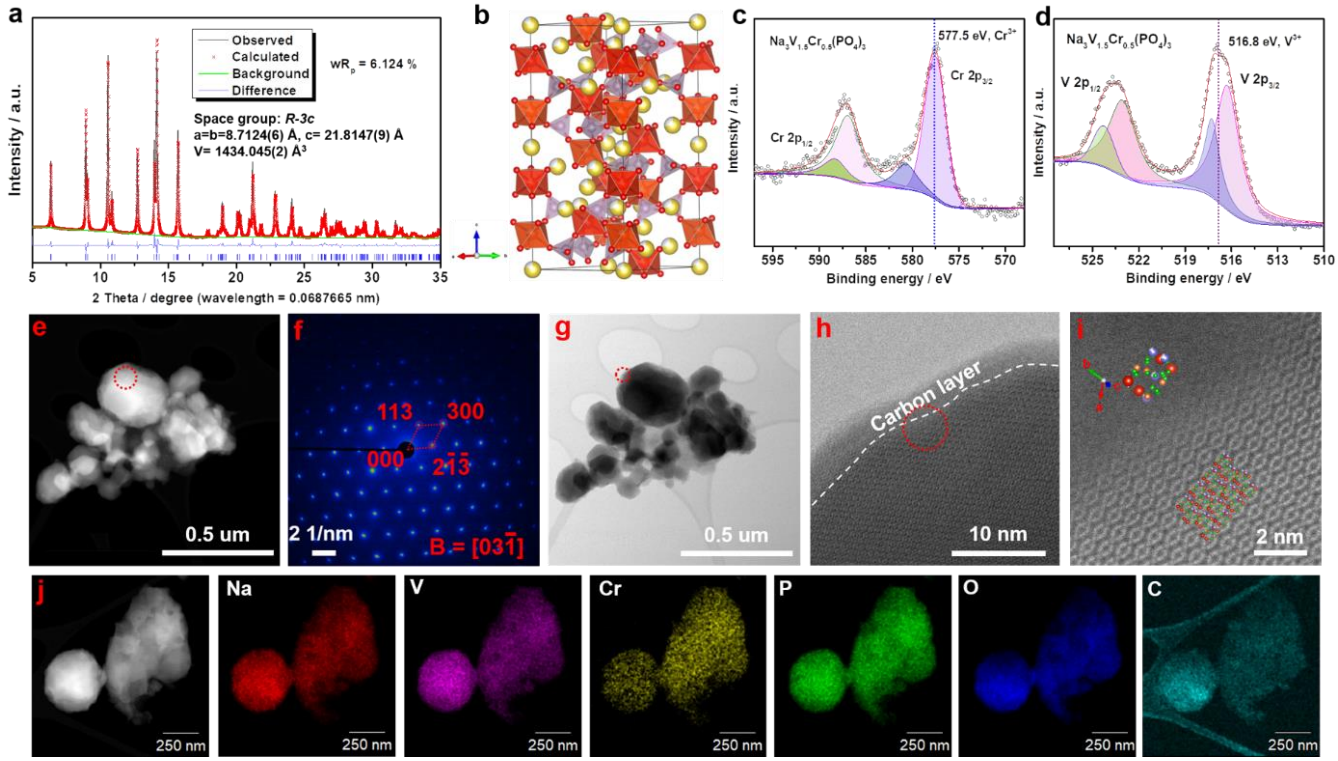

Figure 1 Structural analysis of as-prepared $Na_3V_{1.5}Cr_{0.5}(PO_4)_3$. (**a**) Synchrotron powder diffraction pattern of $Na_3V_{1.5}Cr_{0.5}(PO_4)_3$ with Rietveld refinement results. (**b**) Schematic representation of the refinement results. X-ray photoelectron spectroscopy (XPS) spectra of (**c**) Cr 2p and (**d**) V 2p and the corresponding deconvolution curves of $Na_3V_{1.5}Cr_{0.5}(PO_4)_3$. (**e**) High angle annular dark field (HAADF) image of $Na_3V_{1.5}Cr_{0.5}(PO_4)_3$. (**f**) The corresponding SAED pattern collected from the region marked by the red circle in (**e**). (**g**) The bright field (BF) image of $Na_3V_{1.5}Cr_{0.5}(PO_4)_3$. (**h**) High resolution image of $Na_3V_{1.5}Cr_{0.5}(PO_4)_3$. (**i**) Enlarged HAADF image with the crystal structure as inset. (**j**) Energy dispersive spectroscopy (EDS) mapping results for the detected elements Na, V, Cr, P, O and C.

1s spectra can be deconvoluted into three main peaks, indicating the typical π-bonding graphite-like carbon peaks for delocalized electrons (Figure S3b).[35] The Raman spectra of $Na_3V_{1.5}Cr_{0.5}(PO_4)_3$ is shown in **Figure S4**a. The observed peaks at 362.7 cm^{-1} and 427.8 cm^{-1} can be assigned to the stretching vibrations and bending motions of PO_4 tetrahedra, while the peaks located at 628.3 cm^{-1} is the stretching vibrations of CrO_6/VO_6 octahedra.[45] Also the intensity ratio of D band to G band is observed at 1.03, which indicates the superior electrical conductivity by amorphous carbon on $Na_3V_{1.5}Cr_{0.5}(PO_4)_3$ particle surface since defects, edges, and structural disorders were created based on the sp^2 carbon layers as well as more bonding sites.[46] Similar stretching vibrations and bending motions also can be detected in the Fourier transform infrared (FT-IR) spectra (Figure S4b). Both symmetric and asymmetric bending/stretching vibrations are clearly observed for PO_4 tetrahedra and CrO_6/VO_6 octahedra, which indicates the vibrational mode of this material is typical of polyanionic-type materials in the low wavenumber range.[47]

We employed both the scanning electron microscopy (SEM) and scanning transmission electron microscope (STEM) in order to observe the morphology of the obtained material. **Figure S5**a-c shows the SEM images of the $Na_3V_{1.5}Cr_{0.5}(PO_4)_3$ cathode, and the SEM-EDS mapping results preliminarily reveal the uniform distribution of the detected elements (Figure S5d and e). From the N_2 isotherms as shown in **Figure S6**a, its specific surface area as calculated by the Brunauer–Emmett–Teller (BET) model is 6.89 $m^2\ g^{-1}$, and its pore size is mainly distributed in the 3-5 nm range. Figure 1e shows the high-angle angular dark-field (HAADF) image of $Na_3V_{1.5}Cr_{0.5}(PO_4)_3$, and the corresponding selected-area electron diffraction (SAED) are displayed in Figure 1f. The SAED pattern can be indexed with the observation axis of [00-1], which confirms the high crystallinity of the obtained $Na_3V_{1.5}Cr_{0.5}(PO_4)_3$ with rhombohedral symmetry (*R*-3*c*) after annealing in Ar atmosphere. More detailed structural information can be seen in Figure 1g to i. In Figure 1h, the carbon layer is observed to be 4 nm thick, and the typical HAADF images exhibit an atomic-level structure viewed along specific crystallographic directions (Figure 1i), and the corresponding schematic illustration is also presented as insets. Positions of Na, V, Cr and P heavy atomic columns can be clearly identified since their individual intensity is proportional to the atomic number (*Z*).[48] High-resolution STEM-EDS mapping results further verify that all the elements of Na, V, Cr, P, O, C coexist and are uniformly distributed in the $Na_3V_{1.5}Cr_{0.5}(PO_4)_3$ particle, which is in good agreement with the refined powder diffraction results. For the following comparison, we also obtained the SEM and EDS results of pristine $Na_3V_2(PO_4)_3$ particle, which is shown in **Figure S7**. The $Na_3V_2(PO_4)_3$ material also possesses similar morphology with the uniform distribution of all detected elements consistent with the refined powder diffraction results shown in Figure S1.

To fully explicate the multi-electron reaction of V in the Cr-doped $Na_3V_{1.5}Cr_{0.5}(PO_4)_3$ material, galvanostatic charge-discharge tests were conducted with the half cells using Na metal as anodes. It should be noted that other Cr-doping amounts in V sites also can trigger the higher voltage redox; however, only the 25 % Cr-doped sample shows stable structure and decent electrochemical performance without any additional

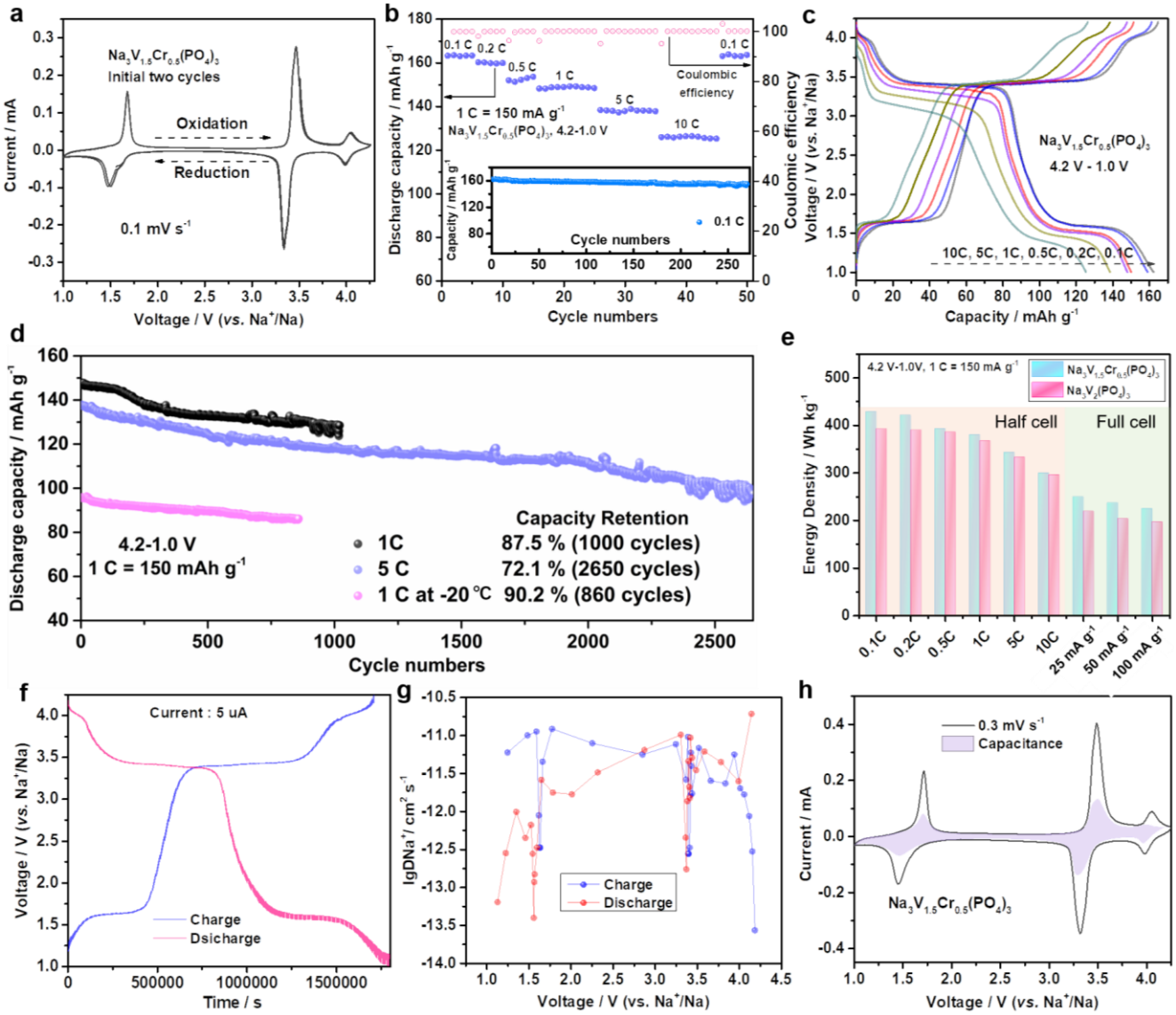

Figure 2 Electrochemical profiles of as-prepared $Na_3V_{1.5}Cr_{0.5}(PO_4)_3$. (**a**) Cyclic voltammetry (CV) curves for the first 2 cycles of $Na_3V_{1.5}Cr_{0.5}(PO_4)_3$ electrode (scan rate 0.1 mV s^{-1}). (**b**) Rate performance from 0.1 C to 10 C (1 C = 150 mA g^{-1}). The inset is the cycling stability at low current density (0.1 C). (**c**) Charge-discharge curves at different rates for the $Na_3V_{1.5}Cr_{0.5}(PO_4)_3$ electrode. (**d**) Long-term cycling stability of the $Na_3V_{1.5}Cr_{0.5}(PO_4)_3$ electrode at 1 C (at room temperature and at -20 ˚C) and 5 C. (**e**) Comparison of the energy density of both the $Na_3V_{1.5}Cr_{0.5}(PO_4)_3$ electrode and the $Na_3V_2(PO_4)_3$ electrode at different C-rates and current densities as half cell and as full cell. (**f**) Galvanostatic intermittent titration technique (GITT) curves of $Na_3V_{1.5}Cr_{0.5}(PO_4)_3$ for both the charge and discharge process. (**g**) Chemical diffusion coefficient of Na^+ ions as a function of voltage calculated from the GITT profile in (**f**). (**h**) The calculated contribution capacitance shown as the shaded area within the CV curve of the $Na_3V_{1.5}Cr_{0.5}(PO_4)_3$ electrode at a scan rate of 0.3 mV s^{-1}.

atoms/sites rearrangements detected after electrochemical activation. The relevant data can be found in **Figure S8** to **Figure S10**. As for our optimum compound $Na_3V_{1.5}Cr_{0.5}(PO_4)_3$, three distinctive oxidation/reduction peaks at 1.6 V, 3.4 V and 4.1 V can be clearly observed in the Cyclic voltammetry (CV) curves during the initial 2 cycles, as shown in **Figure 2**a. These three peaks can be initially assigned to V^{2+}/V^{3+}, V^{3+}/V^{4+} and V^{4+}/V^{5+}, respectively, and detailed analysis will be discussed later. In the voltage window of 4.2 – 1.0 V, the $Na_3V_{1.5}Cr_{0.5}(PO_4)_3$ electrode can exhibit a high reversible specific capacity of 163. 2 mAh g^{-1} at 0.1 C (1 C = 150 mA g^{-1}). Excellent rate performance is also observed while high Coulombic efficiency of nearly 100% is maintained for each cycle (Figure 2b). The inset of Figure 2b displays its superb cycling stability retaining 96.3 % of the initial capacity at 0.1 C for 270 cycles, demonstrating that the robust framework of this Cr-doped polyanionic homologue underwent the least electrochemical degradation. Only small electrochemical polarizations can be observed while increasing C-rates, and the high voltage plateau at 4.1 V is well maintained at all current densities, as illustrated in Figure 2c. In addition, the Cr-doped one, $Na_3V_{1.5}Cr_{0.5}(PO_4)_3$, also exhibits excellent long-term cycling stability. Figure 2d demonstrates the cycling performance at 1 C and 5 C for 1000 cycles and 2650 cycles, respectively, and the corresponding capacity retentions each reach 87.5 % and 72.1 % of the initial capacities. There were no obvious cracks of the electrodes to be found after 2650 cycles

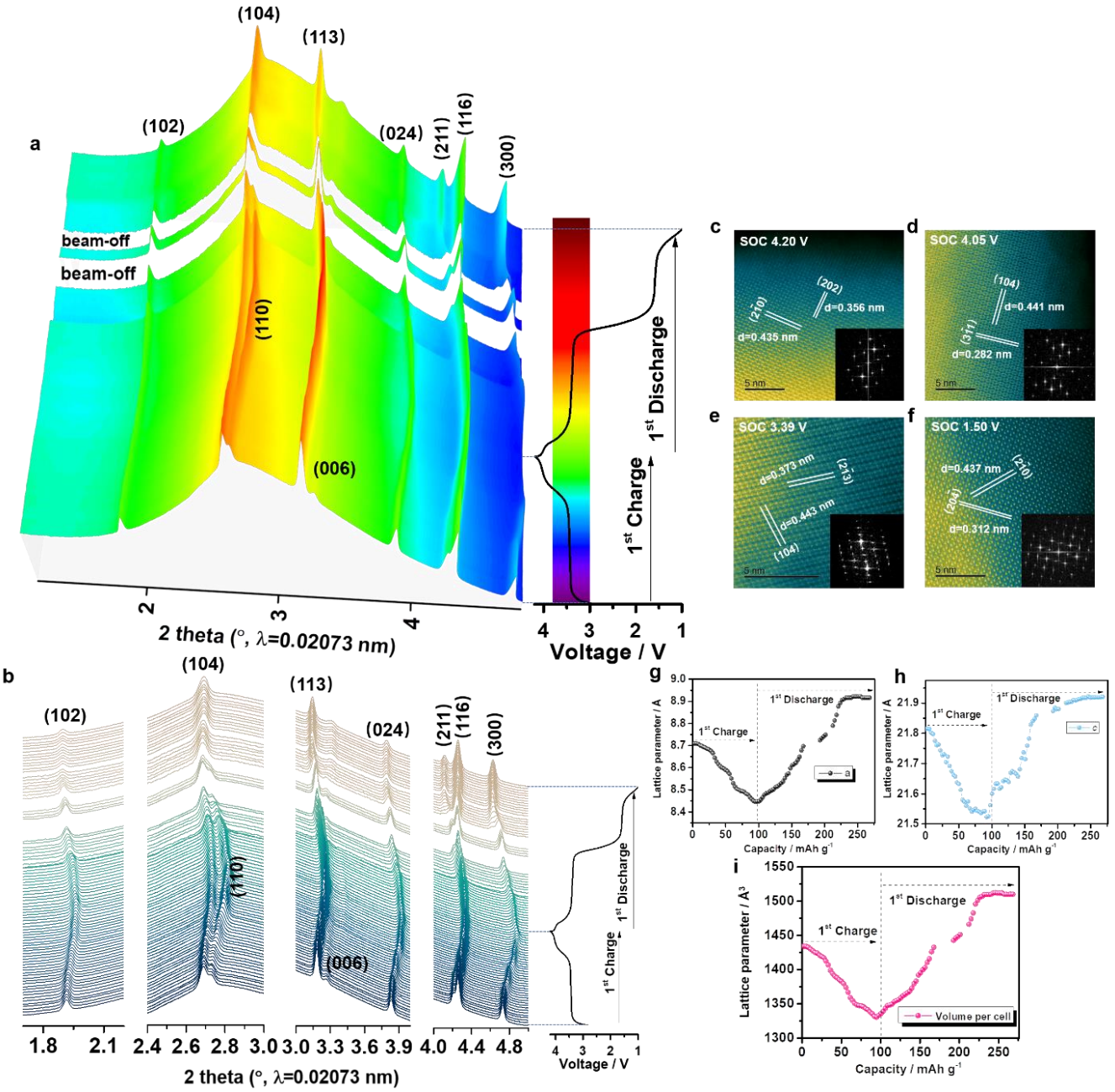

Figure 3 Sodium-storage mechanism study. (**a**) Two-dimensional contour plots and (**b**) stacked line plots of synchrotron-based *operando* XRD patterns of the as-prepared $Na_3V_{1.5}Cr_{0.5}(PO_4)_3$ material with the corresponding 1st charge/discharge profile. HAADF images of the material at a state of charge of (**c**) 4.20 V, (**d**) 4.05 V, (**e**) 3.39 V and (**f**) 1.50 V. Insets: show the fast Fourier transform (FFT) patterns. Variations of crystal parameters of (**g**) *a*, (**h**) *c* and (**i**) volume change per cell.

(**Figure S11**), and the characteristic partial spectra of C, Cr and V were also well maintained even after this huge number of cycles (**Figure S12**). Besides, we also tested its low-temperature performance, and the capacity of 97.5 mAh g^{-1} can be obtained at 1 C under –20 ℃, as well as attaining a capacity retention of 90.2 % after 860 cycles. Also we compared the integrated total energy density values of pristine $Na_3V_2(PO_4)_3$ and Cr-doped $Na_3V_{1.5}Cr_{0.5}(PO_4)_3$, and it is found that thanks to the higher voltage plateau that the V^{4+}/V^{5+} couple provides, the energy densities of $Na_3V_{1.5}Cr_{0.5}(PO_4)_3$ are all slightly higher at various current densities than that of pristine $Na_3V_2(PO_4)_3$ (Figure 2e; the relevant electrochemical profiles of $Na_3V_2(PO_4)_3$ are shown in **Figure S13**). Besides, we also fabricated full cells using hard carbon as the anode (**Figure S14**). The energy densities of $Na_3V_{1.5}Cr_{0.5}(PO_4)_3$//Hard carbon full cell are also higher than that of $Na_3V_2(PO_4)_3$//Hard carbon full cell at various current densities (25 mA g^{-1}, 50 mA g^{-1} and 100 mA g^{-1}, respectively, Figure **S15** and Figure 2e). Therefore, it is very meaningful to fully explore and understand the mechanism for the activation of higher voltage redox couple by doping proper amount of Cr, which possesses great potential for pursuing higher energy densities of SIBs.

The Na diffusion kinetics of $Na_3V_{1.5}Cr_{0.5}(PO_4)_3$ was investigated by means of the galvanostatic intermittent titration technique (GITT) after 30 cycles when it reached its thermal

equilibrium state (Figure 2f). A solid-solution reaction mechanism is observed during the whole process. The theoretical capacity (168 mAh g^{-1}) is calculated based on a three-electron overall reaction, so the sodium diffusion coefficient is a little fluctuated during the continuous de-/insertion procedure. As shown in Figure 2g, the sodium diffusion coefficients are in the range from 10^{-13} to 10^{-10} cm^2 s^{-1} within the voltage window of 1.0– 4.2 V, and there are small coefficient drops at each voltage plateau, which is mainly due to the delayed de-/insertion process at the two-phase regions. The detailed calculation procedure is summarized in **Figure S16**. In addition, the contribution of the capacitance is determined via various scan rates from 0.1 mV s^{-1} to 0.4 mV s^{-1}, as shown in **Figure S17**a. It provides convincing evidence that both the faradic and non-faradic processes always coexist during the charge/discharge process and that they both have positive effects on the overall electrochemical performance. The *b* value was calculated to be around 0.55 for all observed six peaks (Figure S17b), and the non-faradic process (pseudocapacitance behavior) was calculated to be 20.9 % of the total current at 0.3 mV s^{-1} (Figure 2h). This pseudocapacitive behaviour can be regarded as one of the critical factors behind the outstanding electrochemical properties of the Cr-doped homologue, $Na_3V_{1.5}Cr_{0.5}(PO_4)_3$.[49]

peaks are displayed in Figure 3b. The main peaks of (102), (104), (113), (024), (116) and (300) are clearly observed and indexed. It can be seen that all the peaks changed reversibly during the 1st charge and discharge process, indicating that the sturdy polyanionic framework can be well maintained. It should be noted that during the experiment, there were two short periods without beam; however, it does not affect the overall observations and structural analysis. All the observed peaks gradually moved to higher 2θ values during the charge process, and then gradually returned to lower 2θ values upon one more additional sodium insertion compared to the pristine formula ($Na_3V_{1.5}Cr_{0.5}(PO_4)_3$ to $Na_4V_{1.5}Cr_{0.5}(PO_4)_3$). During the fourth sodium ion insertion, there is no obvious angle shift at the end of discharge, indicating the fourth sodium ion insertion does not have much effects on the volume of unit cell. No asymmetric shifts are observed, indicating that there is no crystal distortion or cation migration during sodium de-/insertion process. Both the (104) lattice plane and (110) lattice plane were observed to be shifted to higher angles during sodium extraction, while the (211) peak almost vanished at the end of charge and moved to lower angle during the sodium insertion process. This phenomenon tells us that for the deep sodium insertion/extraction (at the end of charge/discharge), a two-phase sodium storage mechanism is evident.[50] However, unlike

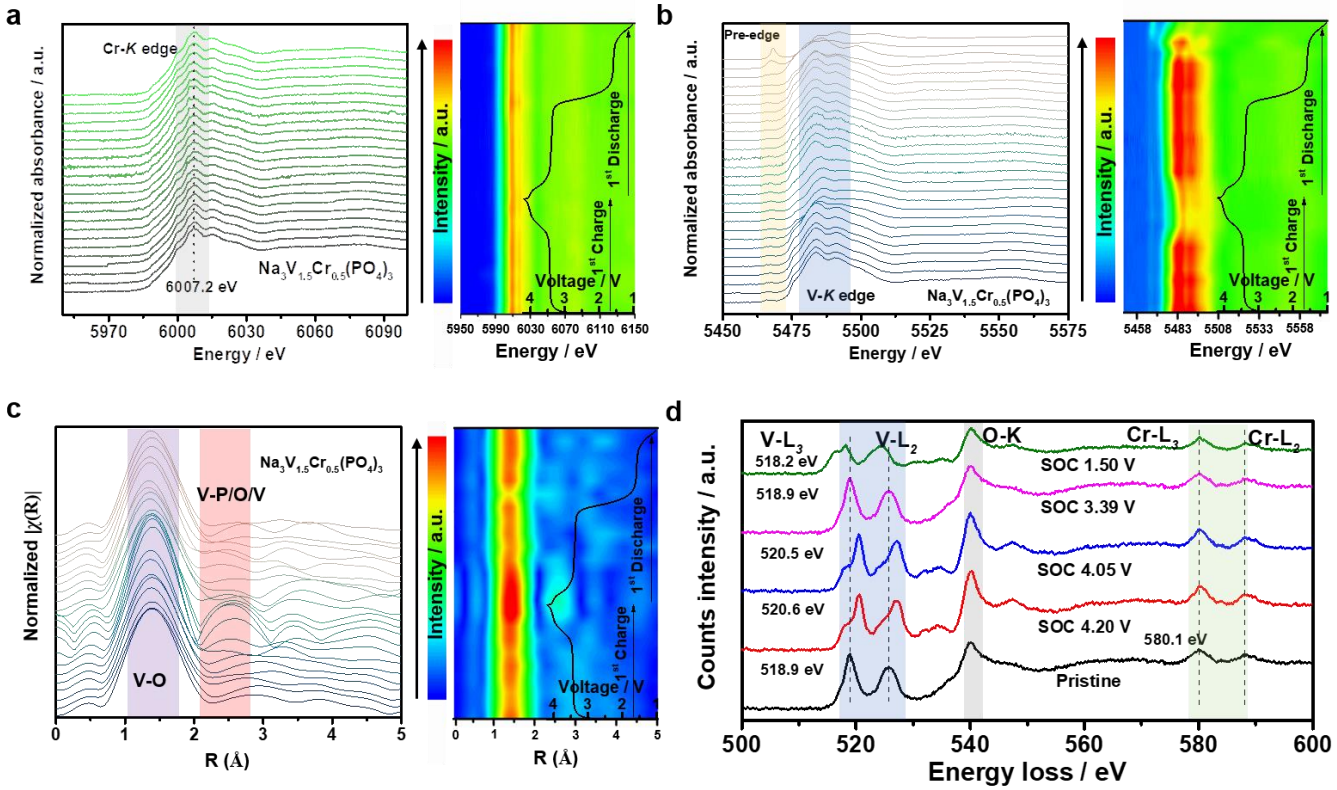

Figure 4 Valence variation characterization of $Na_3V_{1.5}Cr_{0.5}(PO_4)_3$. (**a**) *Operando* XANES spectra and 2D contour plot at the Cr *K*-edge of the $Na_3V_{1.5}Cr_{0.5}(PO_4)_3$ electrode for the first cycle. (**b**) *Operando* XANES spectra and 2D contour plot at the V *K*-edge of the $Na_3V_{1.5}Cr_{0.5}(PO_4)_3$ electrode for the first cycle. (**c**) k^2-weighted Fourier transform magnitudes of V *K*-edge EXAFS spectra. (**d**) *Ex*-situ EELS spectra of V-$L_{2,3}$, O-*K* and Cr-$L_{2,3}$ edge at different states of charge.

In order to fully understand the phase transition and other structural changes of the Cr-doped $Na_3V_{1.5}Cr_{0.5}(PO_4)_3$ having the rhombohedral symmetry, the *operando* synchrotron-based powder diffraction analyses were conducted at DESY Synchrotron, Germany. The whole pattern covering the entire range is shown in **Figure S18**. A whole 3D side view pattern is displayed in **Figure 3**a, and the magnified patterns of selected indexed

the un-doped $Na_3V_2(PO_4)_3$, which possesses an obvious two-phase reaction as previously reported, the major sodium storage of $Na_3V_{1.5}Cr_{0.5}(PO_4)_3$ undergoes a one-phase process (solid solution reaction) at high voltage plateaus of 3.4 V and 4.1 V. This solid solution reaction is beneficial for both fast sodium diffusion and electrochemical reversibility since there is no phase separation stemming from thermodynamic phase

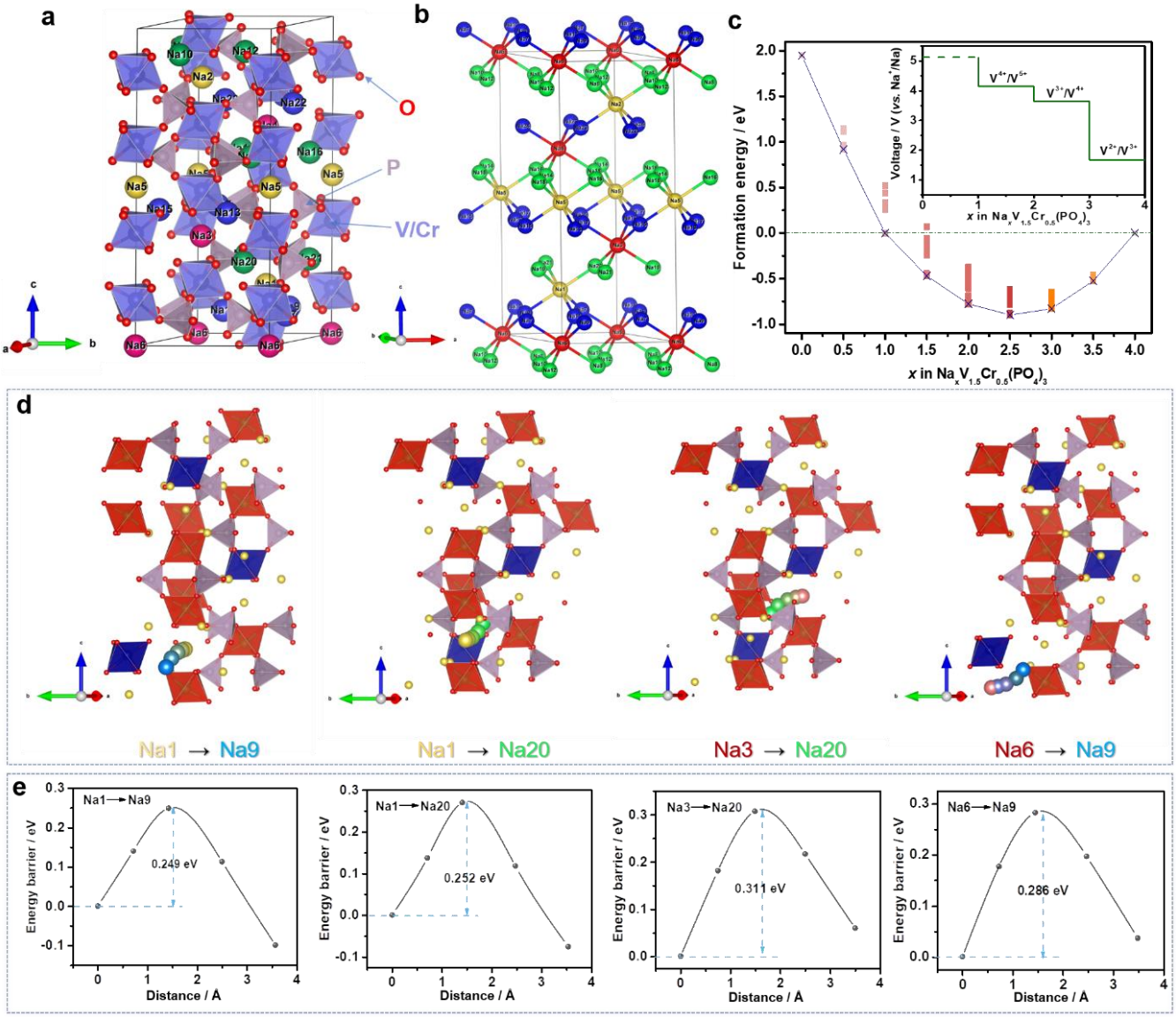

Figure 5 DFT calculation results of possible Na⁺ ion diffusion pathways, and the corresponding migration energy barriers and formation energies in a single unit cell. (**a**) Illustration of the crystal structure of $Na_3V_{1.5}Cr_{0.5}(PO_4)_3$ with four different types of Na ions. (**b**) All of the four types of Na ions in a unit cell. (**c**) Formation energy (convex hull) of $Na_xV_{1.5}Cr_{0.5}(PO_4)_3$ (x = 0, 0.5, 1, 1.5, 2, 2.5, 3, 3.5 and 4) from the DFT study. The inset is the calculated voltage profiles for $Na_xV_{1.5}Cr_{0.5}(PO_4)_3$ (x = 0, 1, 2, 3, and 4). (**d**) Calculated Na⁺ ion diffusion pathways of the A-to-B type (Na1 to Na9), A-to-C type (Na1 to Na20), D-to-C type (Na3 to Na20) and the D-to-B type (Na6 to Na9). (**e**) Corresponding migration energy barriers within the different Na⁺ ion groups as illustrated in (**d**).

instability. Therefore, through the *operando* Synchrotron-based XRD, it is confirmed that both two-phase and solid-solution reactions are involved as the sodium storage mechanism in different states of charge of the Cr-doped homologue. In addition, we also obtained the HAADF images at various states of charge (4.20 V, 4.05 V, 3.39 V, 1.50 V), as shown in Figure 3c to f. Lattice fringes for the (104), (202), (2–10), (3–11), (2–13) and (20–4) planes are clearly observed and identified, indicating the high structural crystallinity of the $Na_3V_{1.5}Cr_{0.5}(PO_4)_3$ during all stages of the electrochemical reactions. The remaining sodium ions (around 34 %) in the unit cell can be regarded as the binding pillars for stabilizing the overall crystal structure. In Figure 3g and h, we have carefully calculated the cell parameters based on the selected peaks during reversible lattice changes. Both the lattice parameter a (= b) and c changed gradually during the charge and discharge process, and the overall change of a and c are 5.6 % and 1.9 %, respectively. Also the unit cell parameter change (7.2 %) is illustrated in Figure 3i. In general, the well-maintained structure and small lattice parameter variations are key factors for the stable long-term cycling stability.

In order to further investigate the valence change as well as redox mechanism of this Cr-doped $Na_3V_{1.5}Cr_{0.5}(PO_4)_3$, both the *operando* X-ray absorption near-edge structure (XANES) and extended X-ray absorption fine structure (EXAFS) analyses were conducted. The XANES spectra at Cr *K*-edge region are shown in **Figure 4**a. During the whole 1st charge and discharge process, no significant shifts can be observed for the Cr *K*-edge XANES spectra, indicating that the doped Cr in $Na_3V_{1.5}Cr_{0.5}(PO_4)_3$ is not involved in the electrochemical reaction and remains at +3 (6007.2 eV) during the whole reaction. Also the peak intensities of both edge and pre-edge regions remain the same, meaning that the CrO_6 octahedra are robust and

did not participate in the charge compensation process. By contrast, the V *K*-edge spectra shift towards the high-energy side during sodium extraction, which indicates an increase in the oxidation state of V (Figure 4b). The peak intensities in the V *K*-edge region decreased at the end of charge, which is possibly due to electron loss in the VO_6 octahedra as well as the shortening of V-O bonds. Hence, the V K-edge spectra moved back to the lower energy region during the following discharge process. At the end of discharge, the pre-edge region is observed to emerge with an obvious pre-peak, suggestive of strong V-O hybridization. According to the galvanostatic charge-discharge curve in the *operando* measurement, the discharge capacity is much larger than the charge capacity, and thus more Na ions are intercalated into the structure after discharge, leading to V^{2+}/V^{3+} redox. These extra Na ions, together with the reduction of V^{3+} to V^{2+} may significantly distort VO_6 octahedra or even change the octahedral symmetry into a tetrahedral symmetry, characterized by the strong V-O hybridization.

We also obtained the *operando* Fourier-transformed (FT) magnitude plot of the V K-edge EXAFS spectra. As shown in Figure 4c, two main peaks are observed with radius of around 1.4 Å and 2.5 Å, which can be assigned to the V-O bond and the V-P/O/V bond. It should be noted that these distances are not the actual bond lengths because these FT

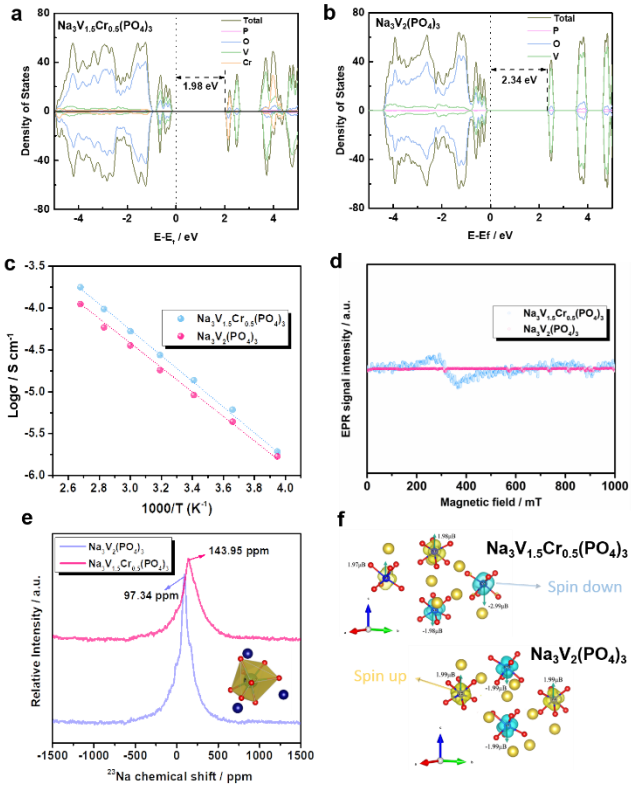

Figure 6 Various analyses disclosing the difference between the pristine and Cr-doped samples. Calculated density of states (DOS) and the corresponding partial density of states (PDOS) diagram of (a) $Na_3V_{1.5}Cr_{0.5}(PO_4)_3$ and (b) $Na_3V_2(PO_4)_3$. (c) The ionic conductivity of both samples. (d) Electron paramagnetic resonance (EPR) spectra of both samples. (e) Solid-state ^{23}Na nuclear magnetic resonance (NMR) spectra for both samples. (f) The comparative electronic spin states for both samples.

spectra were not phase-corrected. There is no obvious V-O bond change during cycling, indicating that the octahedral symmetry was well maintained during the first cycle. However, the peak intensities have undergone a perceptible variation. The peak intensities of both V-O bond and V-P/O/V bond increased at the end of the charge process, which can be ascribed to the shortened atom distance and higher electrostatic repulsion upon deep sodium extraction. In addition, the EXAFS spectrum after one cycle is well overlapped with that of the pristine sample, which means there is almost no V local structural change even with deep sodium insertion. This is consistent with the *operando* XRD results mentioned above. Furthermore, we also employed electron energy-loss spectroscopy (EELS) to verify the valence change as discussed above. The selected areas for collecting the EELS spectra are displayed in **Figure S19**. From Figure 4d, it can be seen that Cr $L_{2,3}$ edge of the pristine $Na_3V_{1.5}Cr_{0.5}(PO_4)_3$ electrode is located at 580.1 eV, and there is no shift at different states of charge. The V $L_{2,3}$ edge changed reversibly from a high energy region to a low energy region, as marked by the dotted line near 519 eV. The same tendency is also observed in the *ex-situ* XPS spectra (**Figure S20**). Therefore, based on the experimental results, it is fully clarified that the Cr dopant in $Na_3V_{1.5}Cr_{0.5}(PO_4)_3$ is totally electrochemically inactive during the charge/discharge process, even if the Cr dopant could successfully activate the high voltage redox couple of V^{4+}/V^{5+} as well as trigger an alternate combined solid-solution reaction.

For fully understanding the superior kinetics and dynamics of the $Na_3V_{1.5}Cr_{0.5(}PO_4)_3$ as well as its intrinsic properties with rhombohedral structure, a density functional theory (DFT) study was conducted. It is found that all the Na^+ ions in a single unit cell can be classified to four different types based on their individual binding energies, as illustrated in **Figure 5**a and b, and they are marked as red, blue, yellow and green, respectively. The detailed calculated information is displayed in Table S3. Using the same fully relaxed model, the formation energies that can further delineate the structural change during sodium extraction is illustrated in Figure 5c. The equation of $E_{form} = E_{Nax} - 0.3334(x-1)E_{Na4} - 0.3334(4-x)E_{Na1}$ is employed to perform the convex hull-like phase diagram per formula unit (E_{form}) with the end member having compositions of $Na_4V_{1.5}Cr_{0.5}(PO_4)_3$ and $Na_0V_{1.5}Cr_{0.5(}PO_4)_3$.[43,44] The calculation step size of x was set at 0.5, and the detailed calculated data are shown in Table S4. The result said that the $Na_{2.5}V_{1.5}Cr_{0.5}(PO_4)_3$ is the most thermodynamically stable phase according to the calculated results, and the intermediate phases from x = 1 to 4 are all metastable phases that can be electrochemically achieved below the convex hull value of zero, which indicates the multi-electron reaction nature of this NASICON-type material. From the lowest energy structures, the sequential reactions based on each metastable phase is also predicted to occur at 4.15 V for V^{4+}/V^{5+}, 3.64 V for V^{3+}/V^{4+} and 1.67 V for V^{2+}/V^{3+}, as shown in the inset image of Figure 5c, and they are all very close to the experimental values. From Figure 5d, the crystal structural images of $Na_3V_{1.5}Cr_{0.5}(PO_4)_3$ illustrate the four different types of Na^+ ions migrating from various typical sodium sites (including A-to-B type, A-to-C type, D-to-C type and D-to-B type). The corresponding energy barriers are displayed in Figure 5e. The well-connected 3D sodium diffusion pathways possess comparatively low energy barriers with the maximum value of 0.311 eV, which is lower than that of the undoped $Na_3V_2(PO_4)_3$, evidencing the superior sodium diffusion kinetics after proper amount of Cr doping. (The energy barriers of the pristine $Na_3V_2(PO_4)_3$ based on similar calculation method are shown in **Figure S21)**.[51,52] This can be considered as one of the

key reasons for the Cr-doped $Na_3V_{1.5}Cr_{0.5}(PO_4)_3$ to trigger the high voltage V^{4+}/V^{5+} redox couple as well as realize higher energy densities even at high current densities.

The NASICON structure is capable of boosting fast ion transportation and accommodating various types of transition metal cations with rich chemical space and tunable electrochemical performance, which is very promising to be the ideal cathode candidate for SIBs. The proper amount of Cr doping can activate the higher redox couple of V^{4+}/V^{5+}, and we have carefully demonstrated its unique properties as above. Therefore, it is of great importance to further explore the in-depth reason of how Cr activates the $V^{4+}/^{5+}$ couple. We first employed DFT to investigate the intrinsic material properties of $Na_3V_{1.5}Cr_{0.5}(PO_4)_3$ and $Na_3V_2(PO_4)_3$ based on their electronic band structures, which are shown in **Figure S22**. For both materials, the conduction band (bottom) and the valence band (top) can be assigned to the same Γ point in the irreducible Brillouin zone. It is found that the band gap of Cr-doped sample is smaller (2.312 eV) than that of the pristine sample (2.664 eV) demonstrating the Cr doping-induced improved capability for carrying both electrons and ions. Besides, the band structure can be divided into two paired lines, which correspond to the ±1/2 spin quantum number (up and down for +1/2 and –1/2).[53] The two paired lines in $Na_3V_2(PO_4)_3$ are well overlapped while in $Na_3V_{1.5}Cr_{0.5}(PO_4)_3$, some lines are not. This phenomenon indicates that a weak magnetic property of $Na_3V_{1.5}Cr_{0.5}(PO_4)_3$ is introduced by Cr doping.

In addition, the calculated density of states (DOS) and the corresponding partial density of states (PDOS) diagram are illustrated in **Figure 6**a and b. The valence bands for both samples consist of the hybridized V 3*d*, P 2*p*, Na 3*s*, and O 1*p* orbitals, and the Cr 3*d* orbital is also observed in $Na_3V_{1.5}Cr_{0.5}(PO_4)_3$ (Figure 6a). Interestingly, the forbidden band gap in $Na_3V_{1.5}Cr_{0.5}(PO_4)_3$ decreased to 1.98 eV compared to the undoped $Na_3V_2(PO_4)_3$ (2.34 eV). The decreased band/energy gaps are attributed to the hybridized Cr 3*d* orbitals, which can be clearly observed in Figure 6a. The Cr dopant ($[Ar]3d^54s^1$) has one more valence electron compared to V ($[Ar]3d^34s^2$), so the unpaired electron can contribute to making the electrical conductivity higher at various temperatures in the local structure (Figure 6c, the corresponding measuring method is illustrated in **Figure S23**), which can be regarded as one of the key reasons for the activated high voltage redox couple V^{4+}/V^{5+}. In order to verify our hypothesis, we conducted dual-mode electron paramagnetic resonance (EPR) spectroscopy on both samples. EPR is a powerful tool to precisely probe the unpaired electron in the structure.[54] The results are shown in Figure 6d. It can be seen that there is no detectable signal response from 0 to 1000 mT of the pristine $Na_3V_2(PO_4)_3$ (V^{III} ions with $t_{2g}^0e_g^0$, S = 0), while a featureless differential signal is clearly observed at around 320 mT of Cr-doped $Na_3V_{1.5}Cr_{0.5}(PO_4)_3$, and it can be assigned to the Cr^{III} ions with $t_{2g}^1e_g^0$ electron configuration (S = 1/2). The EPR result has provided a solid evidence for our hypothesis. Besides, as shown in Figure 6e, the ^{23}Na magic angle spinning (MAS) solid-state nuclear magnetic resonance (NMR) signal of Cr-doped $Na_3V_{1.5}Cr_{0.5}(PO_4)_3$ sample shifts downfield from 97.34 ppm to 143.95 ppm (undoped $Na_3V_2(PO_4)_3$). The observed signal can be assigned to Na(2) and its dipole moment is strongly affected by the surrounding VO_6 or CrO_6 octahedra. The downfield shift of the ^{23}Na signal indicates a higher spinning polarization caused by the unpaired 3*d* electron.[55,56] Similar tendency of upper field shift is also observed in the Raman spectra (higher vibration energy, **Figure S24**), and the intensity ratio of V-L_3 edge to V-L_2 edge of both samples in the EELS spectra (0.971 for $Na_3V_2(PO_4)_3$ and 1.162 for $Na_3V_{1.5}Cr_{0.5}(PO_4)_3$) indicates an increased spinning polarization of 3*d* element of V after Cr doping as well (**Figure S25**). In addition, the electronic spin states comparison extracted from DFT calculation results (Figure 6f) further indicates that the unpaired electron of Cr^{III} ions in Cr-doped $Na_3V_{1.5}Cr_{0.5}(PO_4)_3$ results in asymmetric spin configurations compared to the undoped one, and the variation of spin magnetic moment in the 3*d* orbitals of VO_6 and CrO_6 octahedra activates last remaining valence electron to enable to access the high voltage redox couple $V^{4+/5+}$. All aforementioned characterization results indicate that the unpaired 3d orbital electrons in the electrochemically inactive transition metals can have strong influence on the adjacent sodium ion diffusion as well as the distribution of density of states. We believe that other 3*d* transition metal dopant such as Cu and Mo can also trigger the V^{4+}/V^{5+} redox couple of other polyanionic structures within the current voltage window for higher energy densities.

3. Conclusions

In summary, a comprehensive investigation on the structural and electrochemical properties of Cr-doped $Na_3V_{1.5}Cr_{0.5}(PO_4)_3$ has been carried out. Using the advanced characterization techniques and systematic investigations, we successfully clarified the role of Cr in the rhombohedral structure with clearly activated V^{4+}/V^{5+} redox couple at higher voltage region, resulting in improved energy densities at various C-rates compared to the undoped one. Excellent cycling stability was achieved at a wide voltage window of 4.2–1.0 V (retention of 72.1% after 2650 cycles at 5 C). A reversible solid-solution sodium storage mechanism was observed by *operando* XRD with reduced volume change (~7.2 %), and the Cr dopant remains electrochemically inactive during cycling, as demonstrated by both *operando* XANES and *ex-situ* EELS spectra. Furthermore, the DFT calculation results indicate lowered sodium diffusion barriers in the characteristic well-connected 3D sodium diffusion pathways of NASICON structure through Cr doping. We also disclosed that Cr doping can contribute to the decreased forbidden band gap, and the unpaired electron of Cr in the 3d orbital also can have strong influence on the diffusion of adjacent sodium ions, leading to improved ionic conductivity. Our research highlights the importance of broadly applicable doping strategy for achieving multi-electron reaction of polyanionic cathodes in sodium-ion batteries.

ASSOCIATED CONTENT

Supporting Information. The Supporting Information is available free of charge via the Internet at http://pubs.acs.org."

> XRD patterns; Thermal gravimetric analysis; XPS results; Raman and FT-IR results of $Na_3V_{1.5}Cr_{0.5}(PO_4)_3$ material; SEM and EDS analysis; BET test; Electrochemical profile of $Na_3V_2(PO_4)_3$; Electrochemical profile of hard carbon; Full cell curves; Different CV rates profiles; *Operando* XRD results; Electronic band structure diagram; EIS measurement; EELS spectra (PDF); Electronic band structure; DFT calculations.

AUTHOR INFORMATION

Corresponding Author

*dake1234@korea.ac.kr (Y.-M. Kang)

Author Contributions

M. Chen¶ and W. Hua¶ contributed equally to this work.

Notes

The authors declare no competing financial interest.

ACKNOWLEDGMENT

Y.-M. Kang would like to acknowledge the National Research Foundation of Korea (NRF) grants through the Korean government (NRF-2017R1A2B3004383, NRF-2017R1A5A1015365, 2017M3D1A1039553, and NRF-2020M3D1A1110527 for funding this work. This work was supported by Brain Pool Program through the National Research Foundation of Korea (NRF) funded by the Ministry of Science and ICT (2019H1D3A1A01102899, 2020H1D3A1A02081301). G.-H. Lee acknowledges the financial support from Advanced Light Source (ALS) fellowship program. Additionally, the authors are grateful for the assistance of Pohang Accelerator Laboratory (PAL), National Synchrotron Radiation Research Center (NSRRC, TLC 01) in Taiwan, the Deutsches Elektronen-Synchrotron (DESY) radiation center in Germany.

REFERENCES

(1) Armand, M.; Tarascon, J.-M., Building Better Batteries. *Nature* **2008**, *451*, 652-657.

(2) Davies, D. M.; Verde, M. G.; Mnyshenko, O.; Chen, Y. R.; Rajeev, R.; Meng, Y. S.; Elliott, G. Combined Economic and Technological Evaluation of Battery Energy Storage for Grid Applications. *Nat. Energy* **2018**, *4*, 42-50.

(3) Vaalma, C.; Buchholz, D.; Weil, M.; Passerini, S. A Cost and Resource Analysis of Sodium-Ion Batteries. *Nat. Rev. Mater.* **2018**, *3*, 18013.

(4) Hwang, J. Y.; Myung, S. T.; Sun, Y. K. Sodium-Ion Batteries: Present and Future. *Chem. Soc. Rev.* **2017**, *46*, 3529-3614.

(5) Jin, T.; Li, H.; Zhu, K.; Wang, P. F.; Liu, P.; Jiao, L. Polyanion-Type Cathode Materials for Sodium-Ion Batteries. *Chem. Soc. Rev.* **2020**, *49*, 2342-2377.

(6) Guo, S.; Yi, J.; Sun, Y.; Zhou, H. Recent Advances in Titanium-Based Electrode Materials for Stationary Sodium-Ion Batteries. *Energy Environ. Sci.* **2016**, *9*, 2978-3006.

(7) Zheng, Q.; Yamada, Y.; Shang, R.; Ko, S.; Lee, Y.-Y.; Kim, K.; Nakamura, E.; Yamada, A. A Cyclic Phosphate-Based Battery Electrolyte for High Voltage and Safe Operation. *Nat. Energy* **2020**, *5*, 291-298.

(8) Jo, M. R.; Kim, Y.; Yang, J.; Jeong, M.; Song, K.; Kim, Y. I.; Lim, J. M.; Cho, M.; Shim, J. H.; Kim, Y. M.; Yoon, W. S.; Kang, Y. M. Triggered Reversible Phase Transformation Between Layered and Spinel Structure in Manganese-Based Layered Compounds. *Nat. Commun.* **2019**, *10*, 3385.

(9) Yan, G.; Mariyappan, S.; Rousse, G.; Jacquet, Q.; Deschamps, M.; David, R.; Mirvaux, B.; Freeland, J. W.; Tarascon, J. M. Higher Energy and Safer Sodium-Ion Batteries via An Electrochemically made Disordered $Na_3V_2(PO_4)_2F_3$ Material. *Nat. Commun.* **2019**, *10*, 585.

(10) Chen, M.; Liu, Q.; Hu, Z.; Zhang, Y.; Xing, G.; Tang, Y.; Chou, S. L. Designing Advanced Vanadium-Based Materials to Achieve Electrochemically Active Multielectron Reactions in Sodium/Potassium-Ion Batteries. *Adv. Energy Mater.* **2020**, *10*, 2002244.

(11) Chen, M.; Liu, Q.; Wang, S.-W.; Wang, E.; Guo, X.; Chou, S.-L. High-Abundance and Low-Cost Metal-Based Cathode Materials for Sodium-Ion Batteries: Problems, Progress, and Key Technologies. *Adv. Energy Mater.* **2019**, *9*, 1803609.

(12) Wang, P.-F.; You, Y.; Yin, Y.-X.; Guo, Y.-G. Layered Oxide Cathodes for Sodium-Ion Batteries: Phase Transition, Air Stability, and Performance. *Adv. Energy Mater.* **2017**, *7*, 1701912.

(13) Zhang, K.; Kim, D.; Hu, Z.; Park, M.; Noh, G.; Yang, Y.; Zhang, J.; Lau, V. W.; Chou, S. L.; Cho, M.; Choi, S. Y.; Kang, Y. M. Manganese Based Layered Oxides with Modulated Electronic and Thermodynamic Properties for Sodium-Ion Batteries. *Nat. Commun.* **2019**, *10*, 5203.

(14) Liu, Q.; Hu, Z.; Chen, M.; Zou, C.; Jin, H.; Wang, S.; Chou, S. L.; Dou, S. X. Recent Progress of Layered Transition Metal Oxide Cathodes for Sodium-Ion Batteries. *Small* **2019**, *15*, 1805381.

(15) Chen, M.; Hua, W.; Xiao, J.; Cortie, D.; Chen, W.; Wang, E.; Hu, Z.; Gu, Q.; Wang, X.; Indris, S.; Chou, S. L.; Dou, S. X. NASICON-Type Air-Stable and All-Climate Cathode for Sodium-Ion Batteries with Low Cost and High-Power Density. *Nat. Commun.* **2019**, *10*, 1480.

(16) Chen, M.; Xiao, J.; Hua, W.; Hu, Z.; Wang, W.; Gu, Q.; Tang, Y.; Chou, S. L.; Liu, H. K.; Dou, S. X. A Cation and Anion Dual Doping Strategy for the Elevation of Titanium Redox Potential for High-Power Sodium-Ion Batteries. *Angew. Chem. Int. Ed.* **2020**, *59*, 12076-12083.

(17) Fang, Y.; Liu, Q.; Xiao, L.; Rong, Y.; Liu, Y.; Chen, Z.; Ai, X.; Cao, Y.; Yang, H.; Xie, J.; Sun, C.; Zhang, X.; Aoun, B.; Xing, X.; Xiao, X.; Ren, Y. A Fully Sodiated $NaVOPO_4$ with Layered Structure for High-Voltage and Long-Lifespan Sodium-Ion Batteries. *Chem* **2018**, *4*, 1167-1180.

(18) Song, T.; Yao, W.; Kiadkhunthod, P.; Zheng, Y.; Wu, N.; Zhou, X.; Tunmee, S.; Sattayaporn, S.; Tang, Y. A Low-Cost and Environmentally Friendly Mixed Polyanionic Cathode for Sodium-Ion Storage. *Angew. Chem. Int. Ed.* **2020**, *59*, 740-745.

(19) Chen, M.; Cortie, D.; Hu, Z.; Jin, H.; Wang, S.; Gu, Q.; Hua, W.; Wang, E.; Lai, W.; Chen, L.; Chou, S.-L.; Wang, X.-L.; Dou, S.-X. A Novel Graphene Oxide Wrapped $Na_2Fe_2(SO_4)_3$/C Cathode Composite for Long Life and High Energy Density Sodium-Ion Batteries. *Adv. Energy Mater.* **2018**, *8*, 1800944.

(20) Jiang, L.; Lu, Y.; Zhao, C.; Liu, L.; Zhang, J.; Zhang, Q.; Shen, X.; Zhao, J.; Yu, X.; Li, H.; Huang, X.; Chen, L.; Hu, Y.-S. Building Aqueous K-Ion Batteries for Energy Storage. *Nat. Energy*, **2019**, *4*, 495-503.

(21) Wang, W.; Gang, Y.; Hu, Z.; Yan, Z.; Li, W.; Li, Y.; Gu, Q. F.; Wang, Z.; Chou, S. L.; Liu, H. K.; Dou, S. X. Reversible Structural Evolution of Sodium-Rich Rhombohedral Prussian Blue for Sodium-Ion Batteries. *Nat. Commun.* **2020**, *11*, 980.

(22) Wang, W.; Hu, Z.; Yan, Z.; Peng, J.; Chen, M.; Lai, W.; Gu, Q.-F.; Chou, S.-L.; Liu, H.-K.; Dou, S.-X. Understanding Rhombohedral Iron Hexacyanoferrate with Three Different Sodium Positions for High Power and Long Stability Sodium-Ion Battery. *Energy Storage Mater.* **2020**, *30*, 42-51.

(23) Wang, B.; Han, Y.; Wang, X.; Bahlawane, N.; Pan, H.; Yan, M.; Jiang, Y. Prussian Blue Analogs for Rechargeable Batteries. *iScience* **2018**, *3*, 110-133.

(24) Chen, S.; Wu, C.; Shen, L.; Zhu, C.; Huang, Y.; Xi, K.; Maier, J.; Yu, Y. Challenges and Perspectives for NASICON-Type Electrode Materials for Advanced Sodium-Ion Batteries. *Adv. Mater.* **2017**, *29*, 1700431.

(25) Ni, Q.; Bai, Y.; Wu, F.; Wu, C. Polyanion-Type Electrode Materials for Sodium-Ion Batteries. *Adv. Sci.* **2017**, *4*, 1600275.

(26) Li, H.; Jin, T.; Chen, X.; Lai, Y.; Zhang, Z.; Bao, W.; Jiao, L. Rational Architecture Design Enables Superior Na Storage in Greener NASICON-$Na_4MnV(PO_4)_3$ Cathode *Adv. Energy Mater.* **2018**, *8*, 1801418.

(27) Chen, M.; Zhang, Y.; Xing, G.; Tang, Y. Building High Power Density of Sodium-Ion Batteries: Importance of Multidimensional Diffusion Pathways in Cathode Materials. *Front. Chem.* **2020**, *8*, 152.

(28) Chen, M.; Hua, W.; Xiao, J.; Cortie, D.; Guo, X.; Wang, E.; Gu, Q.; Hu, Z.; Indris, S.; Wang, X. L.; Chou, S. L.; Dou, S. X. Development and Investigation of a NASICON-Type High-Voltage Cathode Material for High-Power Sodium-Ion Batteries. *Angew. Chem. Int. Ed.* **2019**, *59*, 2449-2456.

(29) Gao, H.; Goodenough, J. B. An Aqueous Symmetric Sodium-Ion Battery with NASICON-Structured $Na_3MnTi(PO_4)_3$. *Angew. Chem. Int. Ed.* **2016**, *55*, 12768-12772.

(30) Wang, E.; Xiang, W.; Rajagopalan, R.; Wu, Z.; Yang, J.; Chen, M.; Zhong, B.; Dou, S. X.; Chou, S.; Guo, X.; Kang, Y.-M. Construction of 3D Pomegranate-Like $Na_3V_2(PO_4)_3$/Conducting Carbon Composites for High-Power Sodium-Ion Batteries. *J Mater. Chem. A* **2017**, *5*, 9833-9841.

(31) Guo, J. Z.; Wang, P. F.; Wu, X. L.; Zhang, X. H.; Yan, Q.; Chen, H.; Zhang, J. P.; Guo, Y. G. High-Energy/Power and Low-Temperature Cathode for Sodium-Ion Batteries: *In-situ* XRD Study and Superior Full-Cell Performance. *Adv. Mater.* **2017**, *29*, 1701968.

(32) Wang, E.; Chen, M.; Liu, X.; Liu, Y.; Guo, H.; Wu, Z.; Xiang, W.; Zhong, B.; Guo, X.; Chou, S.; Dou, S.-X. Organic Cross-Linker Enabling a 3D Porous Skeleton-Supported $Na_3V_2(PO_4)_3$/Carbon Composite for High Power Sodium-Ion Battery Cathode. *Small Methods* **2019**, *3*, 1800169.

(33) Wang, D.; Bie, X.; Fu, Q.; Dixon, D.; Bramnik, N.; Hu, Y. S.; Fauth, F.; Wei, Y.; Ehrenberg, H.; Chen, G.; Du, F. Sodium Vanadium Titanium Phosphate Electrode for Symmetric Sodium-Ion Batteries with High Power and Long Lifespan. *Nat. Commun.* **2017**, *8*, 15888.

(34) Zhou, W.; Xue, L.; Lü, X.; Gao, H.; Li, Y.; Xin, S.; Fu, G.; Cui, Z.; Zhu, Y.; Goodenough, J. B. $Na_xMV(PO_4)_3$ (M = Mn, Fe, Ni) Structure and Properties for Sodium Extraction. *Nano Lett.* **2016**, *16*, 7836-7841.

(35) Xu, Y.; Wei, Q.; Xu, C.; Li, Q.; An, Q.; Zhang, P.; Sheng, J.; Zhou, L.; Mai, L. Layer-by-Layer $Na_3V_2(PO_4)_3$ Embedded in Reduced Graphene Oxide as Superior Rate and Ultralong-Life Sodium-Ion Battery Cathode. *Adv. Energy Mater.* **2016**, *6*, 1600389.

(36) Li, X.; Huang, Y.; Wang, J.; Miao, L.; Li, Y.; Liu, Y.; Qiu, Y.; Fang, C.; Han, J.; Huang, Y. High valence Mo-doped $Na_3V_2(PO_4)_3$/C as a high Rate and Stable Cycle-Life Cathode for Sodium Battery. *J Mater. Chem. A* **2018**, *6*, 1390-1396.

(37) Soundharrajan, V.; Alfaruqi, M. H.; Lee, S.; Sambandam, B.; Kim, S.; Kim, S.; Mathew, V.; Pham, D. T.; Hwang, J.-Y.; Sun, Y.-K.; Kim, J. Multidimensional $Na_4VMn_{0.9}Cu_{0.1}(PO_4)_3$/C Cotton-Candy Cathode Materials for High Energy Na-Ion Batteries. *J Mater. Chem. A* **2020**, *8*, 12055-12068.

(38) Yang, C.; Xin, S.; Mai, L.; You, Y. Materials Design for High-Safety Sodium-Ion Battery. *Adv. Energy Mater.* **2020**, *11*, 2000974.

(39) Zhu, T.; Hu, P.; Wang, X.; Liu, Z.; Luo, W.; Owusu, K. A.; Cao, W.; Shi, C.; Li, J.; Zhou, L.; Mai, L. Realizing Three-Electron Redox Reactions in NASICON-Structured $Na_3MnTi(PO_4)_3$ for Sodium-Ion Batteries. *Adv. Energy Mater.* **2019**, *9*, 1803436.

(40) Zhao, Y.; Gao, X.; Gao, H.; Jin, H.; Goodenough, J. B. Three Electron Reversible Redox Reaction in Sodium Vanadium Chromium Phosphate as a High-Energy-Density Cathode for Sodium-Ion Batteries. *Adv. Funct. Mater.* **2020**, *30*, 1908680.

(41) Liu, R.; Xu, G.; Li, Q.; Zheng, S.; Zheng, G.; Gong, Z.; Li, Y.; Kruskop, E.; Fu, R.; Chen, Z.; Amine, K.; Yang, Y. Exploring Highly Reversible 1.5-Electron Reactions ($V^{3+}/V^{4+}/V^{5+}$) in $Na_3VCr(PO_4)_3$ Cathode for Sodium-Ion Batteries. *ACS Appl. Mater. Interfaces* **2017**, *9*, 43632-43639.

(42) Aragón, M. J.; Lavela, P.; Ortiz, G. F.; Tirado, J. L. Benefits of Chromium Substitution in $Na_3V_2(PO_4)_3$ as a Potential Candidate for Sodium-Ion Batteries. *ChemElectroChem* **2015**, *2*, 995-1002.

(43) Wang, J.; Wang, Y.; Seo, D. H.; Shi, T.; Chen, S.; Tian, Y.; Kim, H.; Ceder, G. A High-Energy NASICON-Type Cathode Material for Na-Ion Batteries. *Adv. Energy Mater.* **2020**, *10*, 1903968.

(44) Gao, H.; Seymour, I. D.; Xin, S.; Xue, L.; Henkelman, G.; Goodenough, J. B. $Na_3MnZr(PO_4)_3$: A High-Voltage Cathode for Sodium Batteries. *J Am. Chem. Soc.* **2018**, *140*, 18192-18199.

(45) Fang, Y.; Xiao, L.; Ai, X.; Cao, Y.; Yang, H. Hierarchical Carbon Framework Wrapped $Na_3V_2(PO_4)_3$ as a Superior High-Rate and Extended Lifespan Cathode for Sodium-Ion Batteries. *Adv. Mater.* **2015**, *27*, 5895-5900.

(46) Chen, M.; Chen, L.; Hu, Z.; Liu, Q.; Zhang, B.; Hu, Y.; Gu, Q.; Wang, J.-L.; Wang, L.-Z.; Guo, X.; Chou, S.-L.; Dou, S.-X. Carbon-Coated $Na_{3.32}Fe_{2.34}(P_2O_7)_2$ Cathode Material for High-Rate and Long-Life Sodium-Ion Batteries. *Adv. Mater.* **2017**, *29*, 1605535.

(47) Rajagopalan, R.; Chen, B.; Zhang, Z.; Wu, X. L.; Du, Y.; Huang, Y.; Li, B.; Zong, Y.; Wang, J.; Nam, G. H.; Sindoro, M.; Dou, S. X.; Liu, H. K.; Zhang, H. Improved Reversibility of Fe^{3+}/Fe^{4+} Redox Couple in Sodium Super Ion Conductor Type $Na_3Fe_2(PO_4)_3$ for Sodium-Ion Batteries. *Adv. Mater.* **2017**, *29*, 1605694.

(48) Zuo, W.; Qiu, J.; Liu, X.; Ren, F.; Liu, H.; He, H.; Luo, C.; Li, J.; Ortiz, G. F.; Duan, H.; Liu, J.; Wang, M. S.; Li, Y.; Fu, R.; Yang, Y. The Stability of P2-Layered Sodium Transition Metal Oxides in Ambient Atmospheres. *Nat. Commun.* **2020**, *11*, 3544.

(49) Brezesinski, T.; Wang, J.; Tolbert, S. H.; Dunn, B. Ordered Mesoporous Alpha-MoO_3 with Iso-Oriented Nanocrystalline Walls for Thin-Film Pseudocapacitors. *Nat. Mater.* **2010**, *9*, 146-151.

(50) Jian, Z.; Han, W.; Lu, X.; Yang, H.; Hu, Y.-S.; Zhou, J.; Zhou, Z.; Li, J.; Chen, W.; Chen, D.; Chen, L. Superior Electrochemical Performance and Storage Mechanism of $Na_3V_2(PO_4)_3$ Cathode for Room-Temperature Sodium-Ion Batteries. *Adv. Energy Mater.* **2013**, *3*, 156-160.

(51) Wong, L. L.; Chen, H.; Adams, S. Design of Fast Ion Conducting Cathode Materials for Grid-Scale Sodium-Ion Batteries. *Phys. Chem. Chem. Phys.* **2017**, *19*, 7506-7523.

(52) Hu, P.; Wang, X.; Wang, T.; Chen, L.; Ma, J.; Kong, Q.; Shi, S., Cui., G. Boron Substituted $Na_3V_2(P_{1-x}B_xO_4)_3$ Cathode Materials with Enhanced Performance for Sodium-Ion Batteries. *Adv. Sci.* **2016**, *3*, 1600112.

(53) Ali, M. A.; Murtaza, G.; Laref, A. Exploring Ferromagnetic Half-Metallic Nature of Cs_2NpBr_6 via Spin Polarized Density Functional Theory. *Chin. Phys. B* **2020**, *29*, 066102.

(54) Lau, V. W.; Moudrakovski, I.; Yang, J.; Zhang, J.; Kang, Y. M. Uncovering the Shuttle Effect in Organic Batteries and Counter-Strategies Thereof: A Case Study of the N,N'-dimethylphenazine Cathode. *Angew. Chem. Int. Ed.* **2020**, *59*, 4023-4034.

(55) Li, Q.; Liu, Z.; Zheng, F.; Liu, R.; Lee, J.; Xu, G. L.; Zhong, G.; Hou, X.; Fu, R.; Chen, Z.; Amine, K.; Mi, J.; Wu, S.; Grey, C. P.; Yang, Y. Identifying the Structural Evolution of the Sodium-Ion Battery Na_2FePO_4F Cathode. *Angew. Chem. Int. Ed.* **2018**, *57*, 11918-11923.

(56) Peng, J.; Ou, M.; Yi, H.; Sun, X.; Zhang, Y.; Zhang, B.; Ding, Y.; Wang, F.; Gu, S.; Lo´pez, C. A.; Zhang, W.; Liu, Y.; Fang, J.; Wei, P.; Li, Y.; Miao, L.; Jiang, J.; Fang, C.; Li, Q.; Ferna´ndez-Dı´az, M. T.; Alonso, J. A.; Chou, S.; Han, J. Defect-Free-Induced Na^+ Disordering in Electrode Materials. *Energy Environ. Sci.*, **2021**, *14*, 3130-3140.

Multi-electron reaction of NASICON-type cathode is synthesized and its multi-electron property is systemically investigated as well as role of dopant during sodium storage and valence electrons transition process towards higher energy density sodium-ion batteries.

ToC figure